Reversible and rapid calcium intercalation into molybdenum vanadium oxides

Aniruddha S. Lakhnot[a], Kevin Bhimani[a], Varad Mahajani[b], Reena A. Panchal[a], Shyam Sharma[a] (ORCID), and Nikhil Koratkar[a,b,1]

Looming concerns regarding scarcity, high prices, and safety threaten the long-term use of lithium in energy storage devices. Calcium has been explored in batteries because of its abundance and low cost, but the larger size and higher charge density of calcium ions relative to lithium impairs diffusion kinetics and cyclic stability. In this work, an aqueous calcium–ion battery is demonstrated using orthorhombic, trigonal, and tetragonal polymorphs of molybdenum vanadium oxide (MoVO) as a host for calcium ions. Orthorhombic and trigonal MoVOs outperform the tetragonal structure because large hexagonal and heptagonal tunnels are ubiquitous in such crystals, providing facile pathways for calcium–ion diffusion. For trigonal MoVO, a specific capacity of $\sim$203 mAh g^{-1} was obtained at 0.2C and at a 100 times faster rate of 20C, an $\sim$60 mAh g^{-1} capacity was achieved. The open-tunnel trigonal and orthorhombic polymorphs also promoted cyclic stability and reversibility. A review of the literature indicates that MoVO provides one of the best performances reported to date for the storage of calcium ions.

calcium | aqueous battery | complex oxides | porosity | intercalation

The pervasive impact of lithium (Li)–ion batteries from portable electronics to grid and renewable energy storage is indisputable (1–4). The recent boom in electric vehicles also demands high-performance, affordable, and safer batteries (3). Li–ion batteries have dominated the rechargeable battery market, but the scarcity of Li resources is leading to cost and availability concerns (5, 6). To make affordable and sustainable batteries, earth-abundant metals such as sodium (Na), potassium (K), magnesium (Mg), calcium (Ca), and aluminum (Al) are preferred (7–13). Among these Mg, Ca, and Al metal ions are multivalent in nature, i.e., one ion insertion will deliver two or more electrons per ion during battery operation (9, 14, 15). Thus, to achieve a certain level of specific capacity, the number of ions required to participate in the redox process will be lower for multivalent ions as compared to monovalent ions. Consequently, multivalent ion chemistries have seen increased interest within the academic and industrial battery community. However, ions such as Mg^{2+} and Al^{3+} exhibit high charge density and therefore strongly interact with host ions in the electrode, causing slow solid-state diffusion (16–19). This problem is alleviated to some extent for calcium—the bigger ionic size of Ca^{2+} relative to Mg^{2+} and Al^{3+} enables a lower charge density, and hence it is relatively easier for Ca^{2+} to diffuse within intercalation electrodes (20–23). Furthermore, the reduction potential of Ca^{2+} (−2.87 V vs. the standard hydrogen electrode) is the lowest compared to other candidate multivalent ions, which translates to higher cell voltage and energy density (21, 24).

While Ca^{2+} is easier to intercalate than Mg^{2+} and Al^{3+}, it remains a major challenge to find a high-performing electrode host for Ca^{2+}, due to its large size and the substantial coulombic interaction between incoming Ca ions and host ions within the electrode. Prussian blue analogs have been used as a host for Ca^{2+} because of their large pore sizes (25–30). Layered materials such as vanadium oxide (31) and potassium birnessite (32) have also been examined because of the large spacing between 2-dimensional layers in these materials. Recently, Na super ionic conductor (NASICON) structured materials such as $NaV_2(PO_4)_3$ (33, 34) and $Ca_xNa_{0.5}VPO_{4.8}F_{0.7}$ (35) have been explored for Ca storage because the ionic size of Na is very close to that of Ca ($\sim$1 Å). However, the aforementioned materials either lack high specific capacity, high-rate performance, or cyclic stability. One class of materials that has yet to be explored for Ca–ion intercalation is open-tunnel transition metal oxide structures such as molybdenum vanadium oxide (MoVO) that contain large pores and channels for ion transport (36). Such materials can be synthesized by polyoxometalate (POM)-based chemistries. POMs are large metal oxyanion building blocks, and by controlling reaction conditions (e.g., pH, temperature, pressure), open-channel crystals can be obtained (37–39). For example, Sadakane et al. (37) and Ishikawa and Ueda (38) have synthesized five different phases of MoVO—orthorhombic, trigonal, tetragonal, ε-Keggin POM, and amorphous—by tuning the reaction conditions. While MoVO synthesis by traditional hydrothermal

Significance

Calcium ion intercalation into electrode materials is challenging due to the large size and high charge density of calcium ions relative to lithium. Here, we report oxide structures containing big open spaces (heptagonal and hexagonal channels) as a prospective solution. This could open avenues for high-performing calcium–ion batteries that offer a cost-effective and sustainable alternative to lithium-based batteries.

Author affiliations: [a]Department of Mechanical, Aerospace and Nuclear Engineering, Rensselaer Polytechnic Institute, Troy, NY 12180; and [b]Department of Materials Science and Engineering, Rensselaer Polytechnic Institute, Troy, NY 12180

reaction methods is a time-consuming process, in a recent advance, Kaveevivitchai et al. used microwave synthesis to drastically reduce the reaction time from 48 h to ~1 h (40).

Note that the choice of electrolyte (41) also strongly influences the performance of Ca–ion batteries. First, we consider organic electrolytes. Deploying Ca metal in an organic electrolyte is problematic because an ion-insulating layer forms at the metal/electrolyte interface (13). In a recent breakthrough, reversible Ca plating/stripping was achieved, but the operational temperature was ~100 °C and the coulombic efficiency was low (24). Besides coulombic efficiency and cyclic stability, high-rate capability is also a challenge with organic electrolytes. Organic electrolytes contain relatively large solvent molecules, and hence incoming ions must be de-solvated prior to insertion, which slows down the kinetics (42, 43). Recent work indicates that the cyclic stability and rate performance of Ca–ion batteries can be improved by using electrolytes containing some amount of water (25, 44, 45) or completely water-based (aqueous) electrolytes (46). This is because water molecules need not be de-solvated and can insert along with the solvation sheath of the ion. The presence of water also shields the ionic charge, providing reduced interaction between incoming ions and the host (25, 44–47). The use of aqueous chemistries also eliminates fire hazard, which is an ever-present danger with flammable organic electrolytes.

In this study, we examined the intercalation of Ca into three different polymorphs of MoVO: orthorhombic (ortho), trigonal (tri), and tetragonal (tetra). The study was performed with an aqueous electrolyte containing ~5 m calcium triflate $(Ca(OTf)_2)$. Triflate salts have high solubility in water, and a large salt concentration helps widen the electrochemical stability window, allowing higher voltages to be applied (48–50). Ortho and tri MoVO compounds contain 6,7-membered rings that are 5 Å to 6 Å wide (approximately 3 times bigger than a Ca ion), enabling Ca ions to be inserted in the wide-open channels of the crystal. Both ortho and tri polymorphs in this study demonstrated similar performance, but tetra exhibited rapid capacity decline and reduced coulombic efficiency because of low tunnel size and irreversible loss of Ca. For tri MoVO, the specific capacity at 0.2C was ~203 mAh g^{-1} and at a rate as high as 20C, ~60 mAh g^{-1} was achieved. The open-tunnel crystal structure also promotes improved reversibility and cyclic stability. To gain deeper insight into rate performance, the diffusion of Ca^{2+} in tri MoVO was characterized using cyclic voltammograms (CV), electrochemical impedance spectroscopy (EIS), and galvanostatic intermittent titration technique (GITT) methods. The measured Ca^{2+} diffusion coefficients are orders of magnitude faster than that of multivalent ions such as Mg^{2+} and even faster than Li^{+} diffusion into typical oxide-based electrodes. Ex situ X-ray photoelectron spectroscopy (XPS) and X-ray diffraction (XRD) confirmed the reversibility of Ca^{2+} intercalation and the structural stability of the ortho and tri phases of MoVO. These results showcase the potential of developing open-tunnel transition metal oxide structures to build high-performing Ca–ion batteries that could offer a cost-effective and sustainable alternative to Li-based batteries.

Results and Discussion

A schematic of the synthesis process for ortho MoVO is shown in Fig. 1A. Ammonium molybdate $((NH_4)_6Mo_7O_{24})$ and vanadyl sulfate $(VOSO_4)$ were used as the precursor source for Mo and V, respectively. Solutions were mixed under N$_2$ atmosphere to avoid excess oxygen. The mixed solution was acidic (pH ~3) because the molecules present in the solution belong to the POM class of compounds. POMs are metal-oxo cluster anions that act as building units (B.U.) for structural transformation. Final structure is defined by the arrangements of B.U. and octahedra linkers, which can be tuned by process parameters such as pH, time, temperature, and pressure. In the present case, Mo_6O_{21} was the B.U. (*SI Appendix*, Fig. S1) and the reaction conditions (as described in Fig. 1A), generated ortho MoVO. Tri MoVO was obtained by changing the pH of the mixed solution to ~2.2, and tetra MoVO was derived from ortho MoVO by thermal transformation (heated at ~575 °C for 2 h under N$_2$). The XRD data in Fig. 1B confirms the formation of the desired compounds based on the literature (51). The Rietveld refinement of these XRD patterns is provided in *SI Appendix*, Fig. S2. Fig. 1C–E shows the crystal structure of ortho, tri, and tetra MoVO, respectively. Both the ortho and tri structures contain heptagonal as well as hexagonal voids. These are big micropores (in the 5 Å to 6 Å range), which can accommodate large cations (e.g., Ca^{2+}) and small molecules. On the other hand, tetra is limited to much smaller pentagonal, tetragonal, and trigonal voids. The fourier transform infrared (FTIR) spectrum (*SI Appendix*, Fig. S1) of all three MoVO polymorphs was almost identical, indicating that bonding states and building units were the same, and it is only the arrangement of building units that gave rise to different crystal structures. The XPS spectra of all three polymorphs confirmed the presence of Mo, V, and Oxygen (O) (*SI Appendix*, Fig. S3). Moreover, Mo exists in +6 and +4 oxidation states, whereas V exists in +5 and +4 oxidation states (*SI Appendix*, Fig. S3). The morphology of the samples was examined under scanning electron microscopy (Fig. 1F–H). MoVOs are long rods (4–10 μm) ranging from 400 to 700 nm in diameter. Insets in Fig. 1F-H show energy-dispersive spectroscopy (EDS) mapping, which demonstrates the uniform distribution of Mo, V, and O elements in the rods. Fig. 1I is a typical EDS spectrum of tri MoVO. Multiple samples were characterized to establish its molecular formula, which was estimated as $Mo_{2.5+y}VO_{10+z}$ ($0 < y \leq 0.55$; $0 < z \leq 1.1$); the ortho and tetra phases showed similar stoichiometry.

Electrochemical tests were performed on a custom-built cell (*SI Appendix*, Fig. S4), and activated carbon (AC) was used as a pseudo reference electrode. AC was calibrated (*SI Appendix*, Fig. S5) and exhibited a potential of 3.247 V vs. Ca^{2+}/Ca. The samples were cycled within the electrochemical stability window (*SI Appendix*, Fig. S6) of a 5 m Ca(OTf)$_2$ aqueous electrolyte. Fig. 2A–C represents CV of ortho, tri, and tetra MoVO conducted at 0.1 mV s^{-1}. The CV profile was quite similar for ortho and tri. One notable feature in all CV curves was that the current peak (in the range −0.98 to −1.2 V) during first discharge vanished after the third cycle. This peak is attributable to solid electrolyte interphase (SEI) formation. One broad peak at approximately −0.51 V and another at −1.4 V was observed during discharge for both ortho and tri MoVO (Fig. 2A and B). Three pair of anodic peaks at −0.27, −0.37, and −1.2 V for ortho and −0.26, −0.48, and −1.21 V for tri were also observed. The initial broad peak (at −0.51 V) and corresponding anodic peaks (−0.26 and −0.48 V) occurred because of V reduction. This finding aligns well with V-based cathodes employed in Ca–ion batteries (31, 52). As we discuss later (Fig. 3F), V preferentially reduces in stages (multiple redox mechanism is typical [52–54] of V-based compounds). The initial peak (−0.51 V) corresponded to the V^{+5} to V^{+4} reduction. The peak at −1.4 V/−1.2 V could be attributed to a mix of both the redox process (V^{+4} to V^{+3} reduction) and the capacitive storage mechanism. CV profiles overlapped well after the third cycle, suggesting good reversibility. For tetra MoVO (Fig. 2C), peaks at deeper discharge (−1.2 to −1.4 V) were not detected,
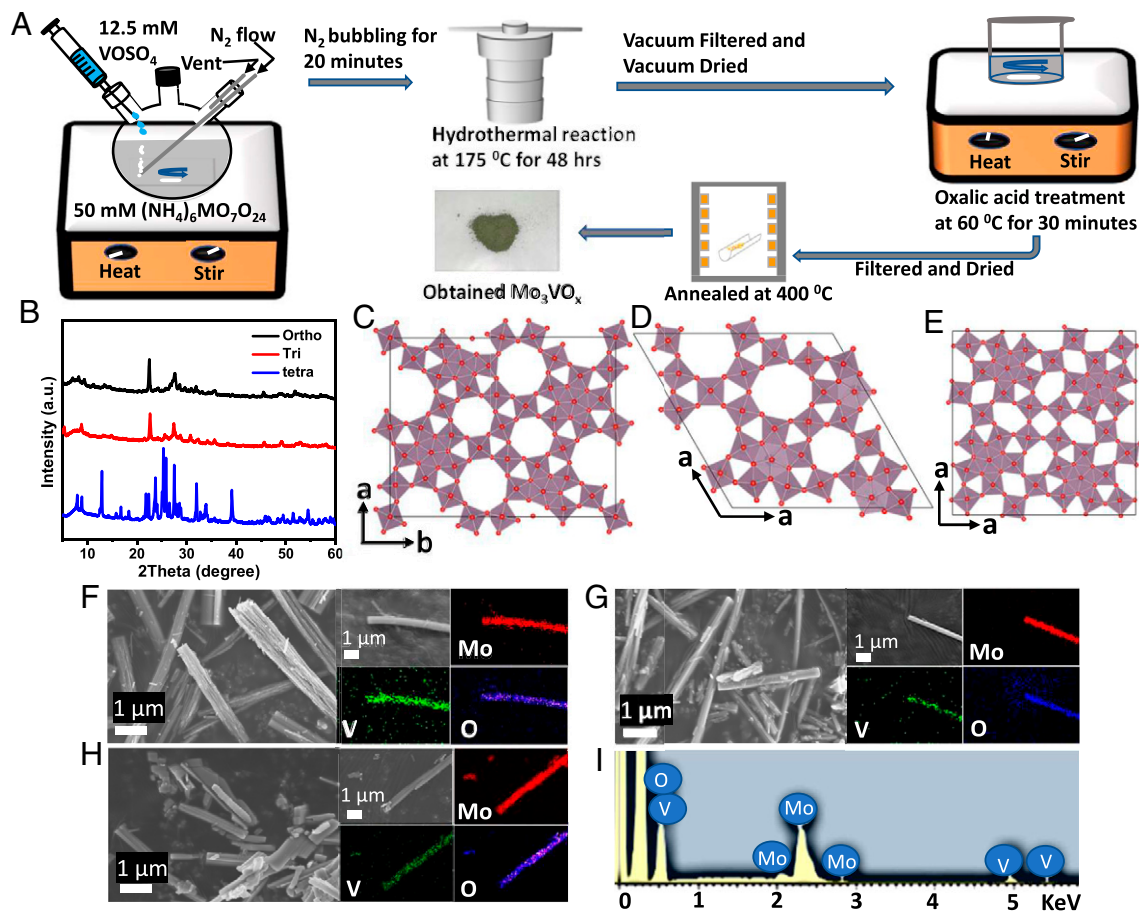
Fig. 1. Synthesis procedure, crystal structure, and characterization of MoVO. (*A*) Schematic of all steps involved in the synthesis of ortho MoVO. Tri MoVO synthesis involves pH adjustment (of precursor solution) to 2.2 using 2M H_2SO_4 and hydrothermal reaction for ~20 h. Tetra MoVO was obtained by annealing ortho MoVO at ~575 °C under N_2 atmosphere. (*B*) XRD for all three MoVO compounds (a.u. denotes arbitrary units). Crystal structure of (*C*) ortho, (*D*) tri, and (*E*) tetra MoVO. Orthorhombic and trigonal structure contains hexagonal and heptagonal tunnels, whereas tetragonal polymorph contains pentagonal, tetragonal, and trigonal tunnels (a, b denote crystallographic axes). Scanning electron microscopy images and EDS mapping of synthesized rods of (*F*) ortho, (*G*) tri, and (*H*) tetra MoVO (Scale bar, 1 μm in all microscopic images). Mapping shows distribution of Mo, V, and Oxygen (O) throughout the rod. (*I*) EDS spectrum of tri MoVO. EDS spectrum for ortho and tetra also exhibited similar peaks for Mo, V, and O.

indicating its lower electrochemical activity. Tetra had much smaller size voids in the structure, limiting capacitive storage as well as Ca–ion intercalation. Moreover, the CV curves for tetra did not overlap well even at the fifth cycle, indicating the irreversible nature of this material.

To further investigate the voltage profile and cyclic stability, batteries were tested using galvanostatic cycling at 100 mA g^{-1} (Fig. 2*D*–*F*). The first cycle voltage profile was very different compared to the rest of the cycles, which corroborates the CV results and is attributed to SEI formation. The discharge voltage plateaus at −0.4 V and −1.2 V were evident in the case of ortho and tri (Fig. 2*D* and *E*). Voltage profiles were repeatable and sustained through to the 100th cycle. Both materials showed a reversible specific capacity of ~165 mAh g^{-1} during initial cycles and retained to ~140 mAh g^{-1} at the end of the 100th cycle. These results reveal the stable and reversible performance of ortho and tri MoVO. For tetra (Fig. 2*F*), the profile was not repeatable, and it degraded drastically during the initial 10 cycles (drop from 120 mAh g^{-1} to 78 mAh g^{-1}) but stabilized in later cycles. The 50th and 100th cycle had a similar voltage profile, delivering a reversible capacity of ~46 mAh g^{-1}. These data indicate that tetra MoVO exhibits irreversible capacity in the initial cycles. This is presumably due to the smaller void size of tetra MoVO, making it challenging for Ca ions to reversibly diffuse in and out of the structure.

The cyclic stability of all three materials is compared in Fig. 2*G* and *H*. For ortho and tri, there was a slight increment in initial capacity that could be because of electrode activation (Fig. 2*G*). For ortho, the specific capacity dropped from ~165 mAh g^{-1} to ~144 mAh g^{-1}, displaying a capacity retention of ~87% at the end of 100 cycles, whereas tri dropped from ~163 mAh g^{-1} to ~138 mAh g^{-1} with a capacity retention of ~85%. Nonetheless, the performance was similar for ortho and tri. With tetra (Fig. 2*G*), the specific capacity drastically dropped from 120 mAh g^{-1} to 46 mAh g^{-1} over the first 35 cycles and then remained stable until the 100th cycle. The reason for its poor performance is evident when coulombic efficiency is compared in Fig. 2*H*. In just two cycles, coulombic efficiency jumped from 84 to 96% for ortho and from 88 to 97% for tri, but when tetra was observed, it took 63 cycles to improve from 54 to 95%. This is a clear indication of high irreversibility in tetra MoVO. Multivalent ions generally find it difficult to migrate through the crystal structure because of their high charge density. When these ions encounter a relatively condensed space (as in tetra MoVO), they are more likely to interact with the host atoms present in the electrode, resulting in a strenuous de-insertion process, which leads to higher irreversibility.

Once the low-rate cyclic stability of ortho and tri was confirmed, we proceeded to test their rate capability. Fig. 2*I* shows the rate capability performance of tri MoVO. A specific capacity of ~203 mAh g^{-1} was obtained at 0.2 C (1C = 150 mA g^{-1}),
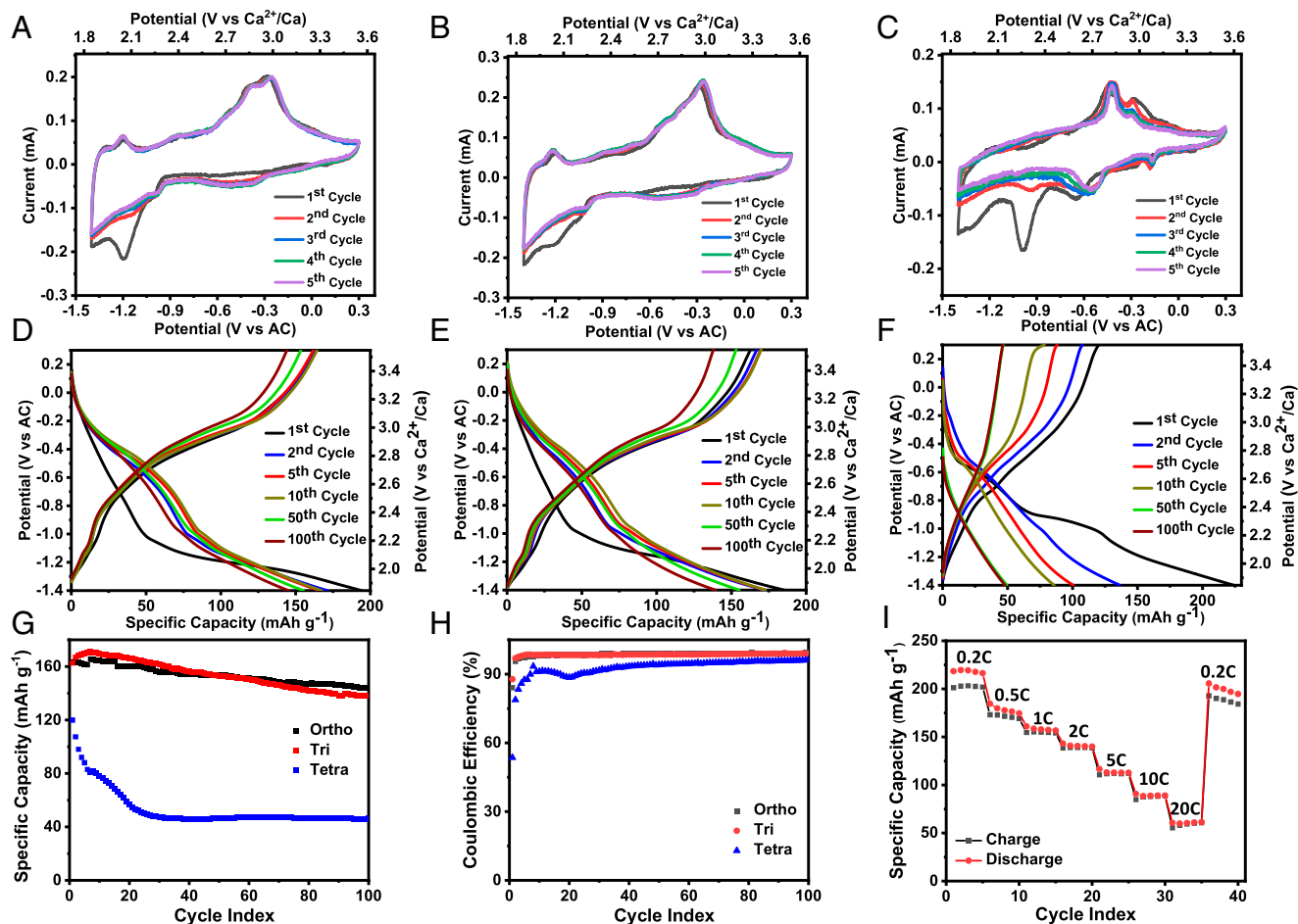
Fig. 2. Electrochemical performance of MoVO compounds in a Ca–ion battery. CV results of (*A*) ortho, (*B*) tri, and (*C*) tetra MoVO performed at 0.1 mv s^{-1}. Five cycles were performed to get a reversible CV profile. Voltage profile acquired using galvanostatic test at 100 mA g^{-1} for (*D*) ortho, (*E*) tri, and (*F*) tetra MoVO. (*G*) Comparison of cyclic stability over 100 cycles among all three polymorphs of MoVO. (*H*) Coulombic efficiency over 100 cycles, revealing superior reversibility for ortho and tri over tetra MoVO. (*I*) Rate capability test results for tri MoVO (1C = 150 mA g^{-1}). Five cycles were performed at each rate to establish stable performance of the compound.

which slowly degraded with rate. The coulombic efficiency was relatively low (~93%) at 0.2C because at a low rate, the electrolyte experiences extreme voltage for a longer duration, resulting in irreversible degradation. Coulombic efficiency improves as the material is cycled at higher rates. Specific capacities of ~113 mAh g^{-1}, ~89 mAh g^{-1}, and ~61 mAh g^{-1} were obtained at C-rates of 5C, 10C, and 20C, respectively. Similar results for high-rate performance were also demonstrated by ortho (*SI Appendix*, Fig. S7). These rate performances are among the highest reported for Ca–ion battery systems. The reason for this performance is presumably the large size and open tunnels available in the crystal structure, enabling the facile diffusion of ions. Another factor that could aid rapid Ca^{2+} intercalation and de-intercalation is that the transition metals (i.e., Mo and V) in MoVO have variable oxidation states and can be reduced to lower oxidation states during Ca^{2+} insertion. This allows for facile charge redistribution, which can help maintain uniform charge neutrality in the material.

To verify that the obtained capacity was because of Ca insertion (and not because of side reactions), electrodes were retrieved from the cycled battery after five charge–discharge cycles, and these were then examined using different characterization tools. We observed no obvious cracks or structural damage on the cycled electrodes (*SI Appendix*, Fig. S8), and the material EDS mapping (Fig. 3*A*) showed a uniform distribution of Ca. Moreover, noticeable peaks of Ca were present in the EDS spectrum (Fig. 3*B*). Similar records were acquired for ortho and tetra MoVO (*SI Appendix*, Fig. S9). To confirm the "bulk" insertion

of Ca, ex situ XRD was performed on the cycled samples. The XRD pattern was retained at all voltages (*SI Appendix*, Fig. S10), which validated the idea that Ca was inserting via intercalation rather than via conversion or alloying. Because of the intercalation reaction, the cyclic stability of these compounds tends to be high. Fig. 3*C* and *D* shows a zoomed-in view of the XRD peaks for (110), (160), and (331) planes. In all cases, with Ca insertion, peak positions shifted toward lower incident angles. A lower Bragg angle signifies an expansion of interplanar spacing. This is to be expected in intercalation–type insertion since the incoming ions tend to expand the unit cell. One salient feature of this study is that when Ca was completely extracted from the samples at 0.3 V, the peak positions also shifted back very close to the original Bragg angle. This reversible shift in peak position confirms that Ca insertion is reversible in tri MoVO.

To further verify the reversibility of calcium insertion, samples at various discharge states were analyzed under XPS (Fig. 3*E*). In the pristine electrode, Ca 2p peaks were obviously absent and began to appear at −0.4 V. The peak became very intense at the maximum discharge state of −1.4 V. When the cell was charged back to 0.3 V, the Ca peak almost disappeared, which verifies the reversible extraction of Ca. High-resolution XPS of V confirmed its active participation in redox reactions (Fig. 3*F*). During the discharge process, from pristine to −0.4 V, the intensity of V^{+4} increased, suggesting that V^{+5} was reducing to V^{+4}. When the voltage was further reduced to −1.4 V, along with V^{+5} reduction, some V^{+4} was also reduced
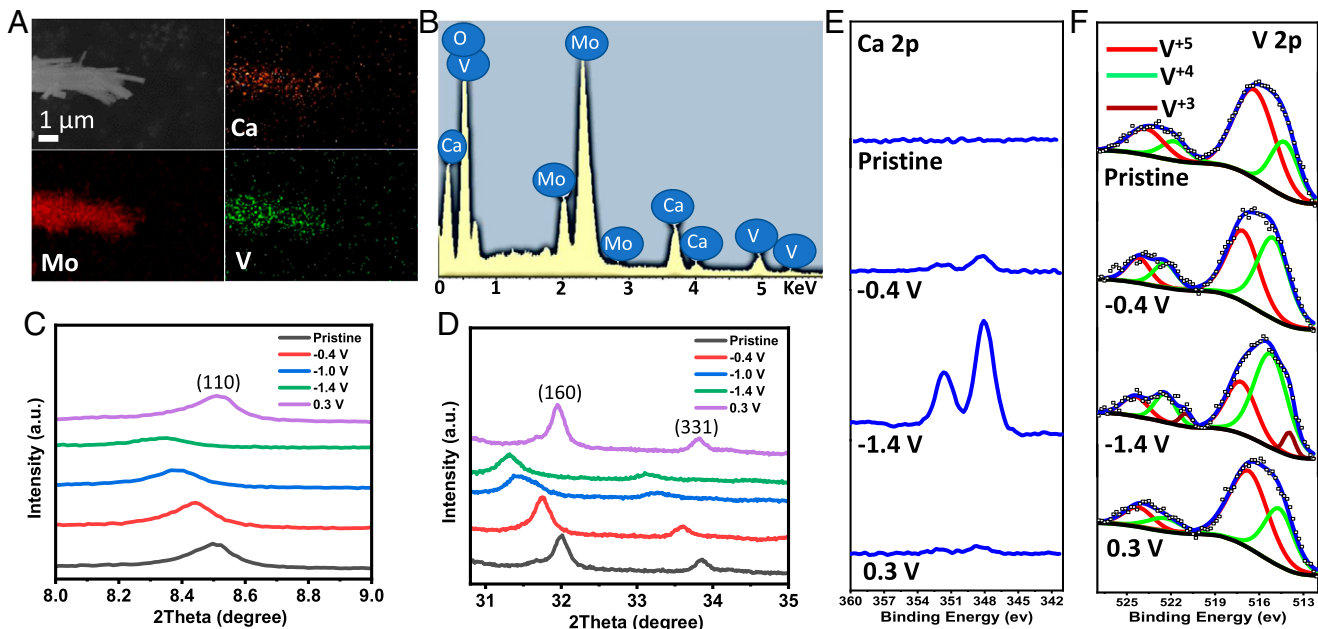
Fig. 3. Ex situ scanning electron microscopy, EDS, XRD, and XPS of tri MoVO. (*A*) Ex situ EDS of tri MoVO at the final discharge state of −1.4 V. Uniform distribution of Ca is visible in the mapping. (*B*) EDS spectrum of this electrode also show peaks corresponding to Ca, Mo, V, and Oxygen (O), confirming that Ca inserts inside the material. XRD peak of Tri MoVO at different voltage values for (*C*) (110), (*D*) (160), and (331) planes (a.u. denotes arbitrary units; parenthetical numbers denote miller indices for the crystal planes). The shift in peak positions indicates that the crystal structure is under strain because of expansion caused by the bulk insertion of calcium. Peaks revert back close to their original positions upon Ca removal, indicating a high degree of reversibility. (*E*) High-resolution XPS spectrum of Ca at different voltages during the discharge–charge cycle. Ex situ study was performed on pristine electrodes, at a discharge potential of −0.4 V, complete discharge at −1.4 V, and finally complete charge at 0.3 V. The appearance of a Ca 2p peak during discharge and disappearance at charge shows high Ca reversibility during the battery cycling process. (*F*) High-resolution XPS spectrum of V at different voltages during the discharge–charge cycle. The reversible change in the oxidation state indicates that V acts as the active redox site.

to V^{+3}. By contrast, there was no appreciable change observed in the oxidation state of Mo (*SI Appendix*, Fig. S11). Hence, we conclude that within the available voltage window, only V serves as an active redox site. The robustness of the MoVO crystal structure was checked by XRD on electrodes after 100 continuous electrochemical cycles. The XRD profile remained the same for all three polymorphs of MoVO (*SI Appendix*, Fig. S12). This substantiates the extreme structural integrity of MoVO compounds, which contributes to their stable cycling performance.

To investigate the high-rate performance of tri MoVO, we studied its kinetic behavior by determining the Ca^{2+} diffusion coefficient. For an initial estimation, the diffusion coefficient was calculated using the Randles–Sevcik equation (55–59):

$$i_p = (2.69 \times 10^5) \, n^{3/2} A D_{Ca}^{1/2} C \nu^{1/2}, \qquad [1]$$

where i_p is the peak current in the CV curve, n is the charge transfer number, A is the surface area of the electrode, D_{Ca} is the diffusion coefficient of Ca, C is the concentration of Ca in the MoVO electrode, and ν is the scan rate. To use Eq. 1, CV was performed at different scan rates as shown in Fig. 4*A*. D_{Ca} for a purely diffusive process can be extracted by performing a linear fit to the peak current vs. the (scan rate)$^{0.5}$ plot. Fig. 4*B* is the plot of the peak current vs. (scan rate)$^{0.5}$ at −0.51 V for the discharge process and at −0.27 V for the charge process. During discharge, D_{Ca} was estimated as 1.07×10^{-10} cm^2 s^{-1}, and during charge, D_{Ca} was 3.2×10^{-10} cm^2 s^{-1}. A similar calculation could not be carried out for the current peak at −1.22 V, since the peak current did not exhibit a linear correlation with (scan rate)$^{0.5}$; rather, the relation could be best fitted by utilizing a power law equation (32, 52, 60, 61):

$$i_p = a\nu^b. \qquad [2]$$

Note that a value of 0.5 for b indicates a purely diffusive process, while a b value of 1 indicates a purely capacitive mechanism. In

Fig. 4*C*, b is 0.77 for the peak current at −1.22 V, which indicates that at this voltage, the storage mechanism in MoVO is a mix of both diffusive and capacitive behavior. To quantify the diffusive and capacitive contributions to the total capacity, we used the following equation (62):

$$i = k_1\nu + k_2\nu^{1/2}. \qquad [3]$$

Here i is the current at a specific potential, ν is the scan rate, $k_1\nu$ represents the capacitive component of the current, and $k_2\nu^{1/2}$ represents the diffusive current. To simplify the calculations, Eq. 3 can be modified as follows:

$$i/\nu^{1/2} = k_1\nu^{1/2} + k_2. \qquad [4]$$

SI Appendix, Fig. S13*A* shows plots of $i\nu^{-0.5}$ vs. $\nu^{0.5}$ to obtain k_1 (results are shown in the plot for five representative voltage values). Such calculations were repeated at various voltage values and were used to generate the capacitive CV curve at 0.5 mV s^{-1} (*SI Appendix*, Fig. S13*B*). The area of the CV curve was used to estimate the contribution of capacitive storage, which was ~25.5%. This resulted in a diffusive contribution of ~74.5% (i.e., a diffusive capacity contribution of ~124 mAh g^{-1}). Thus, while there was a significant capacitive contribution, the diffusive component still dominated the overall capacity. The amount of inserted Ca was also estimated from ex situ EDS results of tri MoVO discharged until −1.4 V (*SI Appendix*, Table S1). The results indicate that 1.3 mol Ca were inserted per formula unit of tri MoVO. This suggests a specific capacity of ~134 mAh g^{-1}, which is comparable to the capacity estimated from the diffusive portion of the CV curve (*SI Appendix*, Fig. S13*B*).

To further determine the diffusion coefficient at different voltage values, EIS was performed at open circuit voltage (OCV), −0.4 V, −1.0 V, and −1.4 V during the discharge process. Fig. 4*D* presents the EIS spectrum of tri MoVO at
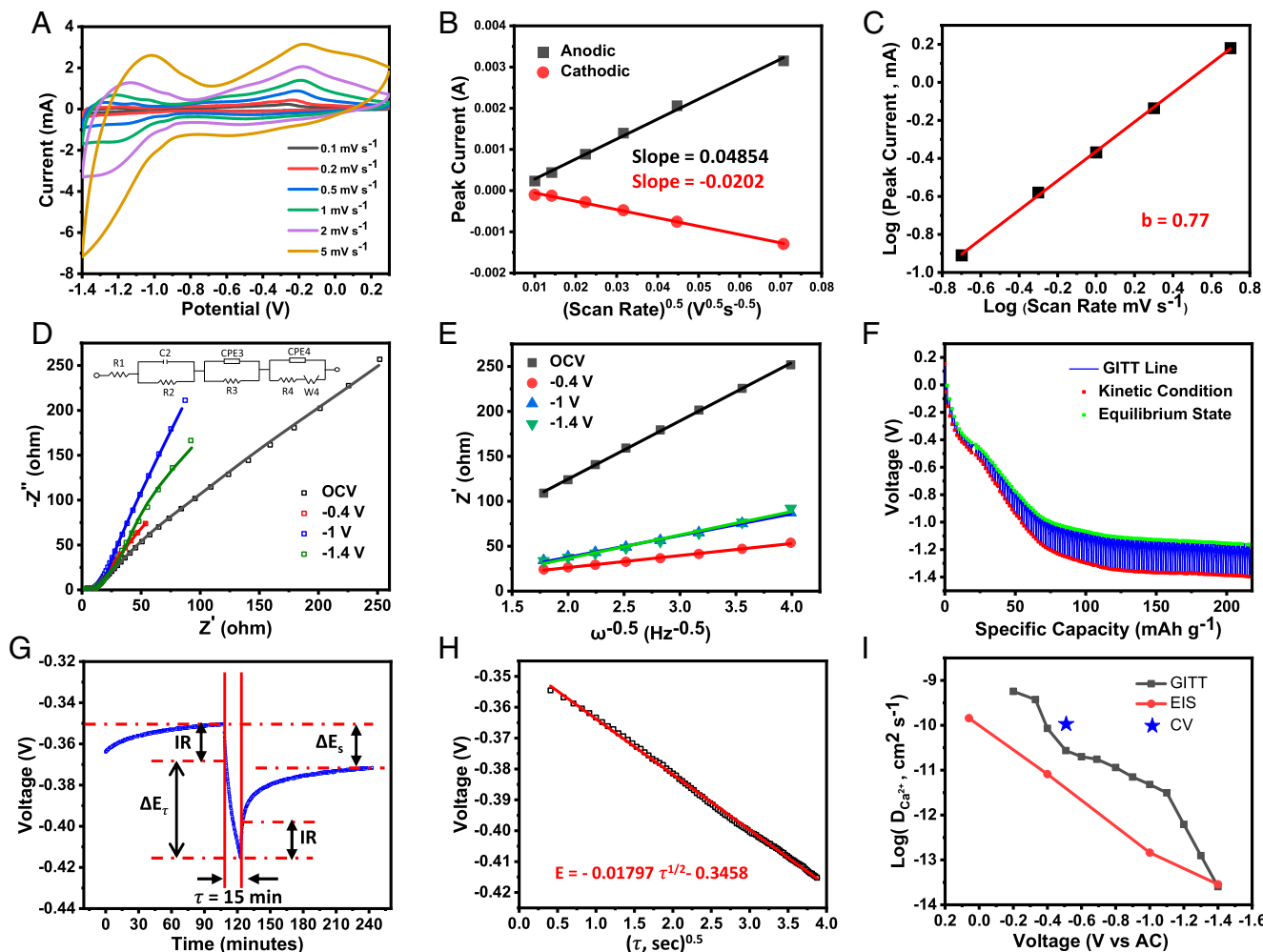
Fig. 4. Diffusion coefficient calculation of Ca^{2+} in tri MoVO. (*A*) CV at different sweep rates. (*B*) Linear fit of peak current vs. (scan rate)$^{0.5}$ at −0.27 V (anodic) and −0.51 V (cathodic) potential. The slopes from these plots were used to calculate the diffusion coefficient using the Randles–Sevcik model. (*C*) Power–law relation between peak current and scan rate at −1.22 V. The "b" value of 0.77 suggests that the storage mechanism contains both diffusive and capacitive contribution and that the Randles–Sevcik equation cannot be applied here. (*D*) EIS of tri MoVO at different voltage values during the discharge process (*Inset*, model used to fit the data). (*E*) Z' (real part of impedance) vs. $\omega^{-0.5}$ at low-frequency regime of EIS. The Warburg factor (σ) was obtained from the slope to calculate the diffusion coefficient. (*F*) Discharge GITT curve of tri MoVO. (*G*) Zoomed-in plot of GITT curve at approximately −0.4 V. Current pulse (τ) of 15 min was applied followed by 2 h relaxation time. IR refers to the ohmic loss. (*H*) Voltage vs. $\tau^{0.5}$ at −0.4 V shows linear relation. (*I*) Calculated Ca^{2+} diffusion coefficient values using CV, EIS, and GITT at different voltage values.

various voltage values; the data were fit by the circuit model described in the inset. For the Nyquist plot, in the high-frequency region, the intercept on the Z' axis corresponds to the solution resistance (R$_s$) and contact resistance of the cell, and the semicircle can be ascribed to the charge transfer (R$_{ct}$) and SEI impedance of the electrodes. A small net resistance of < 9 Ω was registered at all the voltage values, which promoted facile operation of the battery at high C-rates. The oblique feature at the end in the low-frequency regime was associated with the Warburg impedance, which is related to Ca–ion diffusion in the electrode material. To calculate the diffusion coefficient, Eqs. 5 and 6 were used (52, 59, 63–66):

$$D_{Ca} = \frac{R^2 T^2}{2A^2 n^4 F^4 C^2 \sigma^2} \qquad [5]$$

$$Z' = R_s + R_{ct} + \sigma \omega^{-1/2}. \qquad [6]$$

Here, R is the gas constant, T is the absolute temperature, A is the surface area of the electrode, n is the charge transfer number, F is the Faraday constant, C is the concentration of Ca in the material, and σ is the Warburg factor. To calculate the Warburg factor, Eq. 6 was used, which was obtained from the

Z' (real) vs. $\omega^{-0.5}$ plot in the low-frequency regime. The slope of the linear fit between Z' (real) vs. $\omega^{-0.5}$ will yield σ. Fig. 4*E* contained the linear fit at all four voltage values. D$_{Ca}$ at open circuit voltage (OCV) was calculated to be 1.44×10^{-10} cm^2 s^{-1}, which was very close to the value calculated from CV. A similar study was performed on ortho (*SI Appendix*, Fig. S14), and the D$_{Ca}$ for ortho was very close to what was exhibited by tri MoVO.

GITT characterization (Fig. 4*F*) was also carried out to obtain deeper insight into the diffusion process. For this, a current pulse (75 mA g^{-1}) was applied for ∼15 min followed by ∼2 h relaxation time. The maximum absolute voltage during the 15-min period generated by the current pulse accounted for the kinetic condition. On the other hand, the minimum absolute potential achieved after 2 h relaxation represented the equilibrium state. Both the kinetic and equilibrium conditions are highlighted in Fig. 4*F*. The zoomed-in picture of one such current–relaxation cycle at roughly −0.4 V is provided in Fig. 4*G*. When the current pulse was applied, there was a sudden drop in voltage that could be attributed to the resistance drop, and thereafter there was a drop induced by the electrochemical reaction. This change in potential is ΔE$_τ$, regarded as the

change in potential due to kinetic conditions. Subsequently, when the relaxation period began, there was a sudden voltage rise, and then the potential slowly increased and eventually saturated at the end of 2 h. The difference between the saturated potential from the current cycle and the saturated potential from the previous cycle represented the voltage change in the equilibrium condition (ΔE_s). The diffusion coefficient can be calculated by using Eq. 7 (63, 67, 68):

$$D_{Ca} = \frac{4}{\pi\tau} \frac{m^2 V_m^2}{M^2 A^2} \frac{\Delta E_s^2}{\Delta E_\tau^2} \quad \text{for } \tau \ll \frac{L^2}{D}. \qquad [7]$$

Here, m is the mass of active material, V_m is the molar volume of the active material, M is the molar mass of the material, A is the surface area of the electrode, ΔE_s and ΔE_τ have been defined in Fig. 4G, τ is the duration of the current pulse, and L is the diffusion distance. Eq. 7 is valid, if E_τ vs. $\tau^{1/2}$ follows a linear relation, and Fig. 4H validates this condition. Hence, Eq. 7 was applicable for the calculation of diffusion coefficients from the GITT data. Fig. 4I compares the diffusion coefficients retrieved from the EIS and GITT experiments. Both the EIS and GITT results showed the same trend at different voltages, with GITT predicting relatively higher diffusion coefficients. The Ca diffusion coefficient was higher initially (i.e., at the onset of intercalation) and as increasing amounts of Ca-ions were inserted into the material, diffusion was impeded by electrostatic repulsion offered by preoccupied ions. Moreover, there

was reduced nonintercalated volume remaining within the MoVO structure to accommodate more incoming Ca ions. The net result was much lower diffusivity of Ca ions toward the end of the discharge step. The Ca^{2+} diffusion coefficients (Fig. 4I) in the range 5.7×10^{-10} cm^2 s^{-1} to 2.54×10^{-14} cm^2 s^{-1} that we report are orders of magnitude faster than multivalent ions such as Mg^{2+}, which show diffusion coefficients of 10^{-16} to 10^{-19} cm^2 s^{-1} into oxide hosts such as α-MoO_3 and TiO_2 (69, 70). In fact Ca^{2+} diffusion is even faster than Li–ion diffusion (10^{-14} to 10^{-16} cm^2 s^{-1}) into oxide materials such as $Nb_{18}W_{16}O_{93}$ (59), H-Nb_2O_5 (71), TiO_2 (72), and $Li_4Ti_5O_{12}$ (73). These results shed light on the ability of Ca^{2+} to intercalate effectively into tri MoVO at very fast charge/discharge rates of up to 20C (Fig. 2I).

We compared the performance of tri MoVO with various Ca–ion electrode materials reported in the literature. The specific capacity comparison of the various materials at low C-rates is shown in Fig. 5A. The literature from which these data are taken is provided in *SI Appendix*, Table S2. Tri MoVO with a specific capacity of ~203 mAh g^{-1} (at 0.2C) was superior to almost all the reported materials. Because of its relatively large size and high charge density, Ca induced large stresses in the host material, causing structural damage. As a result, several materials lost their capacity in just a few cycles, resulting in a massive capacity fade. The capacity fade rate for various materials tested in Ca–ion batteries is summarized in Fig. 5B. The capacity fade rate per cycle was calculated using Eq. 8:
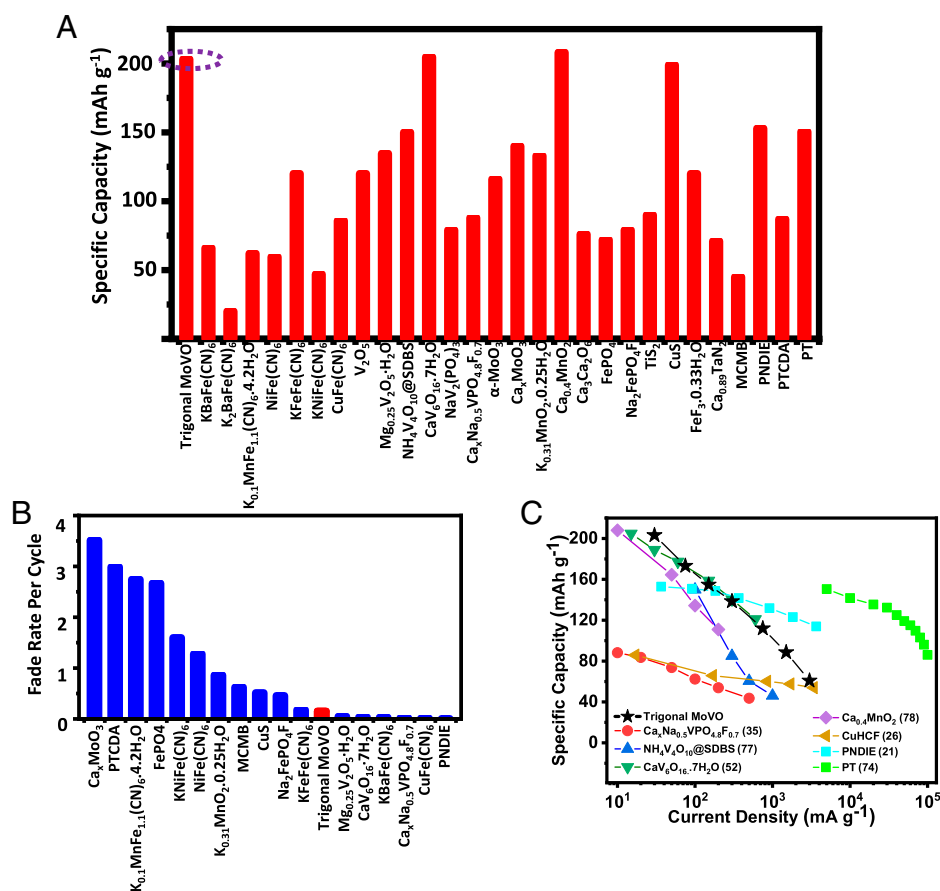

Fig. 5. Tri MoVO performance comparison with the literature for Ca-ion batteries. (A) Specific capacity of tri MoVO (dotted oval) compared with reported materials employed in Ca-ion batteries (*SI Appendix*, Table S2 for full details). SDBS: sodium dodecylbenzenesulfonate; MCMB: mesocarbon microbeads; PNDIE: poly[N,N′-(ethane-1,2-diyl)-1,4,5,8-naphthalenetetracarboxiimide]; PTCDA: perylene-3,4,9,10-tetracarboxylic dianhydride; PT: 5,7,12,14-pentacenetetrone. (B) Percentage fade rate per cycle of various materials tested in Ca-ion batteries (tri MoVO is indicated in red). Literature showing cyclic stability results (*SI Appendix*, Table S2) was used to generate the plot. (C) Specific capacity vs. current density. Articles reporting rate performance have been displayed with reference number denoted in parenthesis.

$$\text{Capacity fade rate per cycle} = \frac{(\text{Initial Capacity} - \text{Final Capacity})}{\text{Initial Capacity}}$$
$$\times 100 \times \frac{1}{\text{Cycle Index}}.$$

[8]

Tri MoVO showed a relatively benign capacity fade rate of ~0.15% per cycle, much lower than a variety of materials including oxides, phosphates, polymers, and Prussian blue analogs (Fig. 5B). Ortho MoVO showed a comparable fade rate (~0.13%) to that of tri. Very few studies have reported rate capability in Ca–ion batteries. The available literature on rate capability is provided in Fig. 5C. Tri MoVO is among the best available materials in terms of delivering high specific capacity over a wide range of current densities. For example, it delivers a specific capacity of ~100 mA h g^{-1} at ~1,000 mA g^{-1} current density. Based on the test data in Fig. 5C, we conclude that 5,7,12,14-pentacenetetrone (PT) (74) is the only material reported to date that shows a far superior rate capability than MoVO; however, it should be noted that the primary charge storage mechanism for PT is capacitive rather than diffusive, and protons also contribute to charge storage in PT (74).

To summarize, we report high–specific capacity and high–rate performing MoVO materials as a host for Ca–ion intercalation in aqueous electrolytes. POM-derived MoVO polymorphs were prepared by hydrothermal processing. Open-crystal structured materials with heptagonal and hexagonal tunnels (ortho, tri) as well as pentagonal tunnels (tetra) were employed in concentrated aqueous electrolyte (5 m Ca(OTf)$_2$). Both ortho and tri demonstrated similar performance, but tetra showed rapid capacity decline and reduced coulombic efficiency because of low tunnel size and irreversible loss of Ca. For tri MoVO, the specific capacity at a low rate of 0.2C was ~203 mAh g^{-1}, and even at a high rate of 20C, a specific capacity of ~60 mAh g^{-1} was retained. The open structure of tri also promoted cyclic stability, demonstrating a capacity fade of ~0.15% per cycle, which was low relative to most oxides, phosphates, polymers, and Prussian blue analogs tested in Ca–ion batteries. To gain deeper insight into the rate performance, the diffusion coefficient of Ca^{2+} was calculated using CV, EIS, and GITT. At the initial stage, inside a relatively empty oxide material, a Ca diffusion coefficient of ~5.7 × 10^{-10} cm^2 s^{-1} was achieved, and it retained a value in excess of 10^{-12} cm^2 s^{-1} in the middle stage of the discharge cycle. These values compare favorably with multivalent ions (such as Mg^{2+}) as well as Li$^+$ insertion into oxide hosts. The reversible insertion and de-insertion of Ca was also confirmed by ex situ EDS, XRD, and XPS characterization. EDS mapping revealed the presence of Ca, whereas XRD indicated the insertion of Ca^{2+} into the bulk electrode structure. XPS analysis at various discharge states demonstrated that during Ca intercalation, V acted as the active redox site whereas Mo remained inert. XPS also verified reversible Ca 2p peaks during charge–discharge cycling. These results indicate a reversible system for Ca–ion intercalation with high specific capacity and rate capability and opens avenues for the deployment of open-crystal structured materials such as MoVO in future energy storage devices.

Materials and Methods

Materials Synthesis. For the synthesis of ortho MoVO, ~40 mL 50 mM (NH$_4$)$_6$Mo$_7$O$_{24}$ (Sigma Aldrich, > 99%) was put in a round-bottom flask. The solution was degassed and then N$_2$ gas was bubbled through the solution with the help of a needle. Another needle was used as a vent. The solution was under vigorous stirring and under N$_2$ atmosphere when ~40 mL 12.5 mM VOSO$_4$

(Sigma Aldrich, 97%) was injected drop by drop using a syringe. Dark purple solution was obtained at the end, which was left for 20 min under N$_2$ bubbling to avoid any excess O$_2$. The resulting solution was quickly transferred to a Teflon container to be placed in a hydrothermal reactor. A hydrothermal reaction was carried out at ~180 °C for ~48 h. Afterwards, the container was left overnight to cool down in the furnace. A greyish precipitate was obtained, which was separated from the solution by vacuum filtration. This filtered product was dried overnight in a vacuum oven at ~80 °C and then treated with oxalic acid (0.4M) at ~60 °C for half an hour. Oxalic acid treatment was performed to get rid of amorphous impurities. The oxalic acid–treated powder was filtered and vacuum dried. In the last step of the synthesis process, the powder was heated in a box furnace at ~400 °C for ~4 h to remove any H$_2$O and NH$_3$ molecules. This processing technique was adopted from the literature (37, 39). Tri MoVO was prepared using the same process as ortho MoVO, except the pH of the dark purple solution (obtained after mixing Mo and V precursors) was adjusted to ~2.2 by dropping ~2 M H$_2$SO$_4$ solution, and the hydrothermal reaction time was only ~20 h. Tetra MoVO was derived from ortho MoVO by heating ortho MoVO at ~575 °C for ~2 h in N$_2$ atmosphere. The heating rate was ~10 °C/min, and the sample was left to cool down under N$_2$. Electrode preparation was identical for all three oxide materials and the activated carbon (4% Ash, Thermo Scientific) electrode. Briefly, the sample, super P conductive carbon, and PVDF (4 wt% in NMP) were mixed in a planetary mixer such that the final composition of slurry(sample: superP: PVDF) had an 80:10:10 percent weight ratio. The slurry was then coated on titanium foil (0.25 mm, 99.99%, Thermo Scientific) for MoVO and on Al foil for activated carbon. Finally, the electrodes were left for drying overnight. Mass loading of MoVO electrodes was 2 to 3 mg cm^{-2} and the electrode thickness was in the range of 25 to 30 μm (*SI Appendix*, Fig. S15). The theoretical density of tri MoVO is 3.7 g ml^{-1}; however, in our case, the particles were submicron sized with 1-dimensional morphology, which resulted in considerable porosity (*SI Appendix*, Fig. S15) at the electrode level. This yielded an electrode density of ~0.87 g mL^{-1}. Such density values, while lower than the theoretical value, are comparable to state-of-the-art graphite, which shows a tap density in the range of 0.2 to 0.8 g mL^{-1} (75, 76). For activated carbon, free-standing film was achieved due to high mass loading (80–100 mg cm^{-2}). Then, 5 m aqueous Ca(OTf)$_2$ (99% min, Thermo Scientific) was used as the electrolyte. To prepare the electrolyte, Ca salt was measured inside an Ar-filled glove box, and HPLC-grade water was quickly added in the ambient.

Materials Characterization. The crystal structure of MoVO particles was confirmed by XRD, which was performed using the Panalytical X'pert PRO MPD system. Cu Kα radiation (λ = 1.54 Å) was used, and a 2-theta range of 5° to 60° was scanned with 0.05° step size. Scanning electron microscopy and EDS mapping was conducted on a Carl Zeiss Supra 55 FESEM to examine morphology, size, and elemental distribution. A Carl Zeiss 1540EsB Crossbeam system was used for scanning electron microscopy (5 kV) and focused ion beam work (Ga ion, 30 kV). XPS was accomplished using Al Kα radiation in a PHI 5000 Versa probe system. XPS analysis was performed after Ar$^+$ ion sputtering for ~15 min to avoid interference from SEI or surface impurities. For ex situ studies, the samples were cycled for five cycles under galvanostatic condition at 100 mA g^{-1} and then held at a particular potential for 15 to 20 h. Afterward, the cells were opened to extract the electrode, thoroughly washed with deionized water, and dried for ~2 h in a vacuum oven at ~80 °C.

Electrochemical Analysis. All electrochemical tests were conducted on a custom-built cell (*SI Appendix*, Fig. S4). Conventional coin cells could not be used because the electrolyte starts to reduce on stainless steel. Nylon/Teflon plates were used because of their mechanical robustness and electrochemical stability. We used 10 sets of hex head bolts and nuts to tightly seal the battery. Activated carbon was used as a pseudo reference electrode. It was calibrated using an LiFePO$_4$ electrode (MTI Corp.). LiFePO$_4$ was first tested against Li$^+$/Li in 1M LiPF$_6$ in EC: DEC (1:1). An insertion potential of 3.475 V was noted against Li$^+$/Li. LiFePO$_4$ was then tested against AC, which demonstrated an insertion potential of 0.048 V against AC. These tests concluded that the AC potential was 3.427 V vs. Li$^+$/Li and hence 3.247 V vs. Ca^{2+}/Ca. Galvanostatic charge–discharge and GITT tests (77,78) were performed on an Arbin BT2000 in

the 0.3 to −1.4 V range. For GITT, a current pulse of 75 mA g^{-1} was applied for 15 min, and a rest period of 2 h was given for relaxation. A voltage stability window of 5 m Ca(OTf)$_2$ was determined using linear sweep voltammetry (LSV) at 1 mV s^{-1}. LSV, CV testing, and EIS were performed on a Gamry Reference 3000 potentiostat. Before conducting EIS at a particular potential, the cell was galvanostatically discharged at 100 mA g^{-1} and then held at the desired potential for ~2 h. EIS was performed by applying an AC signal of 5 mV rms voltage in the frequency range of 100 kHz to 10 mHz.

1. B. Dunn, H. Kamath, J. M. Tarascon, Electrical energy storage for the grid: A battery of choices. *Science (80-.)* **334**, 928–935 (2011).
2. M. Armand, J. M. Tarascon, Building better batteries. *Nature* **451**, 652–657 (2008).
3. K. Amine, R. Kanno, Y. Tzeng, Rechargeable lithium batteries and beyond: Progress, challenges, and future directions. *MRS Bull.* **39**, 395–401 (2014).
4. R. Van Noorden, The rechargeable revolution: A better battery. *Nature* **507**, 26–28 (2014).
5. K. T. Lee, S. Jeong, J. Cho, Roles of surface chemistry on safety and electrochemistry in lithium ion batteries. *Acc. Chem. Res.* **46**, 1161–1170 (2013).
6. S. Komaba et al., Electrochemical Na insertion and solid electrolyte interphase for hard-carbon electrodes and application to Na-ion batteries. *Adv. Funct. Mater.* **21**, 3859–3867 (2011).
7. N. Yabuuchi, K. Kubota, M. Dahbi, S. Komaba, Research development on sodium-ion batteries. *Chem. Rev.* **114**, 11636–11682 (2014).
8. R. Rajagopalan et al., Advancements and challenges in potassium ion batteries: A comprehensive review. *Adv. Funct. Mater.* **30**, 1909486 (2020).
9. H. D. Yoo et al., Mg rechargeable batteries: An on-going challenge. *Energy Environ. Sci.* **6**, 2265–2279 (2013).
10. G. A. Elia et al., An overview and future perspectives of aluminum batteries. *Adv. Mater.* **28**, 7564–7579 (2016).
11. J. Muldoon, C. B. Bucur, T. Gregory, Quest for nonaqueous multivalent secondary batteries: Magnesium and beyond. *Chem. Rev.* **114**, 11683–11720 (2014).
12. R. J. Gummow, G. Vamvounis, M. B. Kannan, Y. He, Calcium-ion batteries: Current state-of-the-art and future perspectives. *Adv. Mater.* **30**, e1801702 (2018).
13. A. Ponrouch, M. R. Palacin, On the road toward calcium-based batteries. *Curr. Opin. Electrochem.* **9**, 1–7 (2018).
14. R. E. Doe et al., Novel electrolyte solutions comprising fully inorganic salts with high anodic stability for rechargeable magnesium batteries. *Chem. Commun. (Camb.)* **50**, 243–245 (2014).
15. J. Muldoon et al., Electrolyte roadblocks to a magnesium rechargeable battery. *Energy Environ. Sci.* **5**, 5941–5950 (2012).
16. Y. Liang et al., Interlayer-expanded molybdenum disulfide nanocomposites for electrochemical magnesium storage. *Nano Lett.* **15**, 2194–2202 (2015).
17. G. G. Amatucci et al., Investigation of yttrium and polyvalent ion intercalation into nanocrystalline vanadium oxide. *J. Electrochem. Soc.* **148**, A940 (2001).
18. E. Levi, M. D. Levi, O. Chasid, D. Aurbach, A review on the problems of the solid state ions diffusion in cathodes for rechargeable Mg batteries. *J. Electroceram.* **22**, 13–19 (2009).
19. D. Aurbach, I. Weissman, Y. Gofer, E. Levi, Nonaqueous magnesium electrochemistry and its application in secondary batteries. *Chem. Rec.* **3**, 61–73 (2003).
20. E. R. Nightingale Jr., Phenomenological theory of ion solvation. *J. Phys. Chem.* **63**, 1381–1387 (1959).
21. S. Gheytani et al., An aqueous Ca-Ion battery. *Adv. Sci. (Weinh.)* **4**, 1700465 (2017).
22. T. Tojo, Y. Sugiura, R. Inada, Y. Sakurai, Reversible calcium ion batteries using a dehydrated Prussian blue analogue cathode. *Electrochim. Acta* **207**, 22–27 (2016).
23. M. Smeu et al., Theoretical investigation of Chevrel phase materials for cathodes accommodating Ca^{2+} ions. *J. Power Sources* **306**, 431–436 (2016).
24. A. Ponrouch, C. Frontera, F. Bardé, M. R. Palacín, Towards a calcium-based rechargeable battery. *Nat. Mater.* **15**, 169–172 (2015).
25. P. Padigi, G. Goncher, D. Evans, R. Solanki, Potassium barium hexacyanoferrate–A potential cathode material for rechargeable calcium ion batteries. *J. Power Sources* **273**, 460–464 (2015).
26. C. Lee, S. K. Jeong, Modulating the hydration number of calcium ions by varying the electrolyte concentration: Electrochemical performance in a Prussian blue electrode/aqueous electrolyte system for calcium-ion batteries. *Electrochim. Acta* **265**, 430–436 (2018).
27. N. Kuperman et al., High performance Prussian blue cathode for nonaqueous Ca-ion intercalation battery. *J. Power Sources* **342**, 414–418 (2017).
28. A. L. Lipson et al., Nickel hexacyanoferrate, a versatile intercalation host for divalent ions from nonaqueous electrolytes. *J. Power Sources* **325**, 646–652 (2016).
29. T. Shiga, H. Kondo, Y. Kato, M. Inoue, Insertion of calcium ion into Prussian blue analogue in nonaqueous solutions and its application to a rechargeable battery with dual carriers. *J. Phys. Chem. C* **119**, 27946–27953 (2015).
30. P. K. Dutta, M. Adil, K. Dutta, S. Mitra, An aqueous Ca-ion full cell comprising BaHCF cathode and MCMB anode. *Chem. Select* **3**, 3687–3690 (2018).
31. Y. Murata et al., Effect of water in electrolyte on the Ca^{2+} insertion/extraction properties of V$_2$O$_5$. *Electrochim. Acta* **294**, 210–216 (2019).
32. J. Hyoung, J. W. Heo, S. T. Hong, Investigation of electrochemical calcium-ion energy storage mechanism in potassium birnessite. *J. Power Sources* **390**, 127–133 (2018).
33. S. Kim et al., High-voltage phosphate cathodes for rechargeable Ca-ion batteries. *ACS Energy Lett.* **5**, 3203–3211 (2020).
34. B. Jeon et al., Reversible calcium-ion insertion in NaSICON-type NaV$_2$(PO$_4$)$_3$. *Chem. Mater.* **32**, 8772–8780 (2020).
35. Z. L. Xu et al., A new high-voltage calcium intercalation host for ultra-stable and high-power calcium rechargeable batteries. *Nat. Commun.* **12**, 1–9 (2021).
36. G. Qu et al., Phase engineering of Mo-V oxides for zinc-ion batteries. [Research Square] [Preprint] (2020). https://www.researchsquare.com/article/rs-94180/v1 (Accessed 30 June 2022).
37. M. Sadakane et al., Assembly of a pentagonal polyoxomolybdate building block, [Mo$_6$O$_{21}$]$_6-$, into crystalline MoV oxides. *Eur. J. Inorg. Chem.* **2013**, 1731–1736 (2013).
38. S. Ishikawa, W. Ueda, Microporous crystalline Mo–V mixed oxides for selective oxidations. *Catal. Sci. Technol.* **6**, 617–629 (2016).
39. T. Konya et al., An orthorhombic Mo$_3$VO$_x$ catalyst most active for oxidative dehydrogenation of ethane among related complex metal oxides. *Catal. Sci. Technol.* **3**, 380–387 (2013).
40. W. Kaveevivitchai, A. Huq, S. Wang, M. J. Park, A. Manthiram, Rechargeable aluminum-ion batteries based on an open-tunnel framework. *Small* **13**, 1701296 (2017).
41. M. Wang et al., Reversible calcium alloying enables a practical room-temperature rechargeable calcium-ion battery with a high discharge voltage. *Nat. Chem.* **10**, 667–672 (2018).
42. D. Kundu et al., Aqueous vs. nonaqueous Zn-ion batteries: Consequences of the desolvation penalty at the interface. *Energy Environ. Sci.* **11**, 881–892 (2018).
43. F. Wang et al., High-voltage aqueous magnesium ion batteries. *ACS Cent. Sci.* **3**, 1121–1128 (2017).
44. J. Song et al., Activation of a MnO$_2$ cathode by water-stimulated Mg$^{(2+)}$ insertion for a magnesium ion battery. *Phys. Chem. Chem. Phys.* **17**, 5256–5264 (2015).
45. P. Novák, R. Imhof, O. Haas, Magnesium insertion electrodes for rechargeable nonaqueous batteries–A competitive alternative to lithium? *Electrochim. Acta* **45**, 351–367 (1999).
46. R. K. Guduru, J. C. Icaza, A brief review on multivalent intercalation batteries with aqueous electrolytes. *Nanomater.* **6**, 41 (2016).
47. R. Y. Wang, C. D. Wessells, R. A. Huggins, Y. Cui, Highly reversible open framework nanoscale electrodes for divalent ion batteries. *Nano Lett.* **13**, 5748–5752 (2013).
48. L. Suo et al., Advanced high-voltage aqueous lithium-ion battery enabled by "water-in-bisalt" electrolyte. *Angew. Chem. Int. Ed. Engl.* **55**, 7136–7141 (2016).
49. F. Wang et al., A rechargeable aqueous Zn^{2+} -battery with high power density and a long cycle-life. *Energy Environ. Sci.* **11**, 3168–3175 (2018).
50. S. Kumar, V. Verma, H. Arora, W. Manalastas, M. Srinivasan, Rechargeable Al-metal aqueous battery using NaMnHCF as a cathode: Investigating the role of coated-Al anode treatments for superior battery cycling performance. *ACS Appl. Energy Mater.* **3**, 8627–8635 (2020).
51. Z. Zhang et al., Zeolitic vanadomolybdates as high-performance cathode-active materials for sodium-ion batteries. *ACS Appl. Mater. Interfaces* **12**, 6056–6063 (2020).
52. L. Liu, Y.-C. Wu, P. Rozier, P.-L. Taberna, P. Simon, Ultrafast synthesis of calcium vanadate for superior aqueous calcium-ion battery. *Research (Wash D C)* **2019**, 6585686 (2019).
53. Y. Liu et al., Facile synthesis of mesoporous NH$_4$V$_4$O$_{10}$ nanoflowers with high performance as cathode material for lithium battery. *J. Mater. Sci.* **53**, 2045–2053 (2018).
54. Y. Ma et al., Synthesis of novel ammonium vanadium bronze (NH$_4$)$_{0.6}$V$_2$O$_5$ and its application in Li-ion battery. *RSC Adv.* **5**, 90888–90894 (2015).
55. C. Park, S. Bin Park, S. H. Oh, H. Jang, W. Il Cho, Li ion diffusivity and improved electrochemical performances of the carbon coated LiFePO$_4$. *Bull. Korean Chem. Soc.* **32**, 836–840 (2011).
56. M. Vujković, I. Stojković, N. Cvjetićanin, S. Mentus, Gel-combustion synthesis of LiFePO$_4$/C composite with improved capacity retention in aerated aqueous electrolyte solution. *Electrochim. Acta* **92**, 248–256 (2013).
57. X. H. Rui, N. Yesibolati, S. R. Li, C. C. Yuan, C. H. Chen, Determination of the chemical diffusion coefficient of Li$^+$ in intercalation-type Li$_3$V$_2$(PO$_4$)$_3$ anode material. *Solid State Ion.* **187**, 58–63 (2011).
58. M. Vujković, M. Mitrić, S. Mentus, High-rate intercalation capability of NaTi$_2$(PO$_4$)$_3$/C composite in aqueous lithium and sodium nitrate solutions. *J. Power Sources* **288**, 176–186 (2015).
59. W. Ye et al., Highly efficient lithium container based on non-Wadsley-Roth structure Nb$_{18}$W$_{16}$O$_{93}$ nanowires for electrochemical energy storage. *Electrochim. Acta* **292**, 331–338 (2019).
60. D. A. Agyeman, K. Song, G. H. Lee, M. Park, Y. M. Kang, Carbon-coated Si nanoparticles anchored between reduced graphene oxides as an extremely reversible anode material for high energy-density Li-ion battery. *Adv. Energy Mater.* **6**, 1600904 (2016).
61. L. Zhang et al., In operando mechanism analysis on nanocrystalline silicon anode material for reversible and ultrafast sodium storage. *Adv. Mater.* **29**, 1604708 (2017).
62. P. Yu, C. Li, X. Guo, Sodium storage and pseudocapacitive charge in textured Li$_4$Ti$_5$O$_{12}$ thin films. *J. Phys. Chem. C* **118**, 10616–10624 (2014).
63. Y. S. Lee, K. S. Ryu, Study of the lithium diffusion properties and high rate performance of TiNb$_6$O$_{17}$ as an anode in lithium secondary battery. *Sci. Rep.* **7**, 16617 (2017).
64. C. Heubner, M. Schneider, A. Michaelis, Investigation of charge transfer kinetics of Li-intercalation in LiFePO$_4$. *J. Power Sources* **288**, 115–120 (2015).
65. T. F. Yi et al., Synthesis and application of a novel Li$_4$Ti$_5$O$_{12}$ composite as anode material with enhanced fast charge-discharge performance for lithium-ion battery. *Electrochim. Acta* **134**, 377–383 (2014).
66. T. Piao, S. Park, C. Doh, S. Moon, Intercalation of lithium ions into graphite electrodes studied by AC impedance measurements. *J. Electrochem. Soc.* **146**, 2794–2798 (1999).
67. K. Tang, X. Yu, J. Sun, H. Li, X. Huang, Kinetic analysis on LiFePO$_4$ thin films by CV, GITT, and EIS. *Electrochim. Acta* **56**, 4869–4875 (2011).
68. X. H. Rui, N. Ding, J. Liu, C. Li, C. H. Chen, Analysis of the chemical diffusion coefficient of lithium ions in Li$_3$V$_2$(PO$_4$)$_3$ cathode material. *Electrochim. Acta* **55**, 2384–2390 (2010).
69. L. F. Wan, J. T. Incorvati, K. R. Poeppelmeier, D. Prendergast, Building a fast lane for Mg diffusion in α-MoO$_3$ by fluorine doping. *Chem. Mater.* **28**, 6900–6908 (2016).
70. T. Koketsu et al., Reversible magnesium and aluminum ions insertion in cation-deficient anatase TiO$_2$. *Nat. Mater.* **16**, 1142–1148 (2017).

71. M. V. Reddy et al., Studies on the lithium ion diffusion coefficients of electrospun Nb_2O_5 nanostructures using galvanostatic intermittent titration and electrochemical impedance spectroscopy. *Electrochim. Acta* **128**, 198–202 (2014).

72. W. L. Wang, J. Y. Park, V. H. Nguyen, E. M. Jin, H. B. Gu, Hierarchical mesoporous rutile TiO_2/C composite nanospheres as lithium-ion battery anode materials. *Ceram. Int.* **42**, 598–606 (2016).

73. F. Wunde, F. Berkemeier, G. Schmitz, Lithium diffusion in sputter-deposited $Li_4Ti_5O_{12}$ thin films. *J. Power Sources* **215**, 109–115 (2012).

74. C. Han, H. Li, Y. Li, J. Zhu, C. Zhi, Proton-assisted calcium-ion storage in aromatic organic molecular crystal with coplanar stacked structure. *Nat. Commun.* **12**, 2400 (2021).

75. MatWeb, TIMCAL TIMREX KS44 primary synthetic graphite. https://www.matweb.com/search/datasheettext.aspx?matguid=fde407c9c3044d12acaad2ef397d44e4. Accessed 30 June 2022.

76. K. J. Griffith, K. M. Wiaderek, G. Cibin, L. E. Marbella, C. P. Grey, Niobium tungsten oxides for high-rate lithium-ion energy storage. *Nature* **559**, 556–563 (2018).

77. T. N. Vo, H. Kim, J. Hur, W. Choi, I. T. Kim, Surfactant-assisted ammonium vanadium oxide as a superior cathode for calcium-ion batteries. *J. Mater. Chem. A Mater. Energy Sustain.* **6**, 22645–22654 (2018).

78. X. Tang et al., A universal strategy towards high-energy aqueous multivalent-ion batteries. *Nat. Commun.* **12**, 2857 (2021).